Nanoscale Advances

rsc.li/nanoscale-advances

ROYAL SOCIETY
OF CHEMISTRY

MINIREVIEW
Michael Hsiao *et al.*
Novel monodisperse FePt nanocomposites for T2-weighted
magnetic resonance imaging: biomedical theranostics
applications

NCNST

Nanoscale Advances

Check for updates

Novel monodisperse FePt nanocomposites for T2-weighted magnetic resonance imaging: biomedical theranostics applications

Zhi-Xuan Chang,†[a] Chien-Hsiu Li, [iD] †[b] Yu-Chan Chang, [iD] [c] Chi-Ying F. Huang, [iD] [ad] Ming-Hsien Chan [iD] *[b] and Michael Hsiao [iD] *[be]

Given the high incidence and mortality of cancer, current research is focused on designing efficient diagnostic methods. At present, clinical diagnoses are made based on X-ray, computed tomography, magnetic resonance imaging (MRI), ultrasound, and fiber optic endoscopy. MRI is a powerful diagnostic tool because it is non-invasive, has a high spatial resolution, uses non-ionizing radiation, and has good soft-tissue contrast. However, the long relaxation time of water protons may result in the inability to distinguish different tissues. To overcome this drawback of MRI, magnetic resonance contrast agents can enhance the contrast, improve the sensitivity of MRI-based diagnoses, increase the success rate of surgery, and reduce tumor recurrence. This review focuses on using iron-platinum (FePt) nanoparticles (NPs) in T2-weighted MRI to detect tumor location based on dark-field changes. In addition, existing methods for optimizing and improving FePt NPs are reviewed, and the MRI applications of FePt NPs are discussed. FePT NPs are expected to strengthen MRI resolution, thereby helping to inhibit tumor development.

1. Introduction

Magnetic resonance imaging (MRI) is commonly used for cancer diagnosis, and contrast agents (CAs) play a vital role in MRI applications.[1–3] For MRI analysis, the hydrogen nuclei must return to the equilibrium state from the excited state and align with the main magnetic field. This phenomenon causes two independent relaxation processes with different time constants: T1 and T2 relaxation. T1 relaxation depends on the alignment of the hydrogen nucleus with the main magnetic field. In contrast, T2 relaxation is related to the disappearance of the phase coherence of the hydrogen nucleus when the external magnetic field is turned off. MRI analysis methods based on these two relaxation processes have their own suitable CAs. Many T1- or T2-weighted MRI CAs based on Gd^{3+}, Mn^{2+}, and iron nanoparticles (NPs) such as iron oxide (Fe_3O_4) NPs have been developed to improve imaging contrast.[4–6] Most clinically used MRI CAs work

by shortening the T1 and/or T2 relaxation time of protons inside tissues, causing the signal strength of the T1-weighted image to increase or the signal strength of the T2-weighted image to decrease. Several T1-weighted CAs based on Gd^{3+} ion complexes have been widely used in clinical practice.[7] However, low-dose compounds/drugs usually have short circulation times in the body and produce a certain degree of toxicity. These drugs may cause side effects such as nephrogenic systemic fibrosis and brain deposits. Therefore, researchers have sought other MRI CAs based on candidate materials such as superparamagnetic NPs, particularly iron-based NPs.[8] In the past few decades, some iron-based T2-weighted CAs have been used in clinical trials or been approved by the U.S. Food and Drug Administration (FDA).[9] Fe_3O_4 in iron-based NPs is already used as a commercial T2-weighted MRI contrast agent.[10] However, its main drawbacks are the agglomeration of NPs, wide particle size distribution, and poor zeta potential value.[11] Fe_3O_4 NPs also lack good colloidal stability, and the repulsive force is insufficient to prevent aggregation.[12] This problem can be attributed to the problems caused by the reaction time and temperature of Fe_3O_4 NPs during the co-precipitation process. Controlling the synthesis procedure is necessary to stabilize Fe_3O_4 NPs and reduce their size by modifying their surface with biocompatible materials.

In contrast, FePt has better colloidal stability. Its uniform size distribution is more suitable as a T2-weighted MRI contrast agent. In the presence of oleic acid and oleylamine stabilizers, monodisperse FePt NPs are synthesized by reducing platinum acetylacetonate and the decomposition of iron pentacarbonyl.

[a]*Institute of Biopharmaceutical Sciences, National Yang Ming Chiao Tung University, Taipei 112, Taiwan*

[b]*Genomics Research Center, Academia Sinica, Taipei 115, Taiwan. E-mail: ahsien0718@gate.sinica.edu.tw; mhsiao@gate.sinica.edu.tw*

[c]*Department of Biomedical Imaging and Radiological Sciences, National Yang Ming Chiao Tung University, Taipei 112, Taiwan*

[d]*Institute of Clinical Medicine, National Yang Ming Chiao Tung University, Taipei 112, Taiwan*

[e]*Department of Biochemistry College of Medicine, Kaohsiung Medical University, Kaohsiung 807, Taiwan*

† Both authors contributed equally to this manuscript.

The composition of FePt NPs is easy to control, the size can be adjusted in the range of 3 to 10 nm in diameter, and the standard deviation is less than 5%.[13] However, due to the inherent dark signal of NPs and MRI sensitivity artifacts, it is difficult to distinguish small, early-stage tumors from hypolipidemic areas.[14–16] Therefore, the clinical applications of these iron-based NPs remain limited. This problem has prompted scientists to consider accumulating more MRI CAs in specific target tissues (*e.g.*, tumor tissues).[17–19] For instance, to develop MRI CAs that can target specific tissues, NPs have been modified with specific antibodies that allow the NPs to easily penetrate the centers of lesions to improve the MRI image contrast.[20–22] Magnetic NPs (MNPs) can enhance image contrast and carry cargos such as chemotherapeutic drugs to monitor the development of diseases during treatment and make treatment decisions in real-time.[23–25]

2. FePt NPs as MRI CAs

MNPs have attracted considerable attention because of their magnetic susceptibility, biocompatibility, stability, and other advantages. MNPs mainly include metal oxide NPs (*e.g.*, Fe_3O_4),[26] metal NPs (*e.g.*, Fe and Co),[27] and metal alloys (*e.g.*, FePt and FeCo).[28] Fe_3O_4 NPs have many advantages as MRI CAs, including strong superparamagnetism, good biocompatibility, easy biodegradability, and simple synthesis. Therefore, Fe_3O_4 NPs have been used in MRI-based diagnosis and treatment.[29–31] However, when used alone, Fe_3O_4 NPs are quickly cleared by the liver and spleen due to their size.[32] Metal alloy NPs with better magnetic properties, such as FePt NPs, have received increasing attention from many researchers. FePt NPs can exhibit excellent superparamagnetism and have chemical stability against oxidation. In addition, FePt nanoparticles with adjustable size and shape can be prepared and modified for different biomedical applications.[33–35] FePt NPs have three different lattice structures: disordered face-centered cubic, ordered face-centered tetragonal and L10 phase. Existing methods for synthesizing FePt nanostructures include physical techniques such as mechanical deformation, arc melting, vacuum evaporation (sputtering and thermal evaporation), laser ablation, chemical methods, physical/chemical methods and electrodeposition. FePt NPs are more stable against oxidation than FeCo NPs and have the advantage of maintaining long-term stability.[36] The sizes and shapes of FePt NPs can be adjusted for various uses in biomedicine.[37–39] The modification of FePt NPs can help improve the T2 image contrast and effectively reduce the side effects, resulting in better MRI CA candidates. This review article compiles the research progress made related to FePt NPs and their application as MRI CAs.

3. Toxicity assessment of FePt NPs

Compared with other inorganic nanomaterials, the key to applying iron-based NPs such as Fe_3O_4 NPs and FePt NPs in essential clinical research lies in the natural integration of such NPs into physiological tissues.[40] Through human tissue proteins such as ferritin, transferrin, and hemosiderin, iron and its oxides can be metabolized, stored, and transported in the organism.[41–43]

The magnetic moment of Fe_3O_4 NPs will uniformly separate under an external magnetic field but agglomerate without the magnetic force. By comparison, FePt NPs with a particle size of less than 10 nm exhibit a single magnetic domain and have superparamagnetic properties like Fe_3O_4 NPs, increasing their diversified clinical applications in medicine. The FePt NPs can disperse in a simulated biological environment without an external magnetic field, which has expanded their diversified clinical applications in medicine. Based on recent research, the main potential concern is the application of NPs in biomedicine.[44–47] The toxicity of NPs is mainly attributed to the following: (1) the results are confusing and contradictory due to the inconsistent experimental standards; (2) the surface properties and size of the NPs will affect the toxicity by affecting the distribution in organs and metabolic time; (3) cell experiments: the results of animal experiments cannot be extended to humans; (4) the long-term toxicity is difficult to detect and study. The organism itself can relieve the toxicity of NPs, such as using protein crowns and liver and kidney metabolism.[48] On the whole, the toxicity of NPs is relatively low compared to organic solvents, including carcinogenicity, immunotoxicity, and genotoxicity.[49]

After the organism degrades FePt NPs, it is mainly metabolized by separating iron ions from platinum. The FDA has approved the low toxicity of iron ions for use in humans for decades, so the main concern is the toxicity of platinum. Platinum itself is very similar to gold, with good biocompatibility, no biological toxicity, and chemical stability. Iron is a metal with excellent magnetic properties, so FePt nano-alloy particles combine the advantages of both. Nanomedicine research has as far as possible through various cell and biological experiments proved that the biocompatibility is good. However, when performing experiments, only a tiny amount of NPs is injected. The selected materials do not contain highly toxic elements, so it is easy to obtain non-toxic results through experiments. In many cases, the dispersibility of NPs directly affects the data results, and vascular embolism caused by aggregated NPs is the leading cause of death in experimental animals. This phenomenon also shows that more research is needed to confirm that these nanomaterials are non-toxic and can be used in clinical medicine. Thus, the carcinogenicity, immunotoxicity, and genotoxicity of NPs require more experiments in the future to give answers to claim they are "safe."

4. Application of FePt NPs as MRI CAs in biomedical diagnosis and treatment

FePt NPs have high crystallinity, suitable magnetic properties, and uniform sizes, which help avoid their rapid removal from the body and thus improve MRI contrast. Modifying the FePt NP surface can effectively improve the biocompatibility, dispersion, and stability of the NPs for biological applications. For instance, adding gold (Au), silicon dioxide (SiO_2), and graphite shells can increase biostability. The addition of degradable biological polymers, including dextran, polyester acid, proteins, and amphiphilic polymers such as polyethylene glycol (PEG), can facilitate the quick dispersion of FePt NPs in the simulated biological environment (Table 1).

Table 1 Various composite FePt NP materials have been used in biological MRI applications. This table lists the advantages obtained by different modifications to FePt NPs in terms of dispersion, diagnosis, stability, therapeutic, targeting, and biocompatibility

Advantage	Modification	Particle size (DLS)	r_2 value (MRI)	Cell type	Reference
Dispersion	Polymaleic anhydride polymer	6 nm	113 mM^{-1} s^{-1} (1.5T)	Cervical cancer (HeLa)	Slabu et al.[50]
	CdS quantum dots/ glutathione (GSH)	353 ± 10 nm	538.1 s^{-1} mg^{-1} mL (600 MHz)	RAW 264.7 cells	Jha et al.[51]
Diagnosis	MnO/DSPE-PEG5000-folate (FA)	33.65 nm	8.14 mM^{-1} s^{-1} (3T)	Breast cancer (4T1 and MCF-7) Liver cancer (HepG2) Cervical cancer (HeLa)	Yang et al.[52]
	Kaolinite/doxorubicin (DOX)	200 nm	29.32 mM^{-1} s^{-1} (4.7T)	Liver cancer (HepG2)	Chan et al.[53]
	F-MoS$_2$	4 nm	n/a	Breast cancer (MCF-7)	Hu et al.[54]
	Metal–organic framework (MOF)	About 100 nm	12.999 mM^{-1} s^{-1}	HepG2, HeLa, BRL-3A, L02, and MCF-7	Meng et al.[55]
Stability	Fe$_2$O$_3$-PEG-FA/DOX	51 nm	91.9 mM^{-1} s^{-1} (3 T)	Epidermoid carcinoma Cervical cancer (KB)	Liu et al.[46]
	Fe$_3$O$_4$-PEG	25.9 nm	99.2 Hz mg^{-1} mL (9.4T)	Breast cancer (4T1.2-neu)	Yang et al.[56]
	Fe$_3$O$_4$	17.8 nm	411.3 mM^{-1} s^{-1} (4.7T)	Epidermoid carcinoma Cervical cancer (KB)	Yang et al.[57]
	DOPAC (3,4-dihydroxyphenylacetic acid)	81.1 nm	131.5 mM^{-1} s^{-1} (9.4T)	n/a	Kim et al.[58]
Therapeutic	SiO$_2$/Au	40 nm	47 mM^{-1} s^{-1} (2.35T)	Bladder cancer (RT4)	Kostevšek et al.[59]
	Graphene oxide (GO) nanocomposites	3–4 nm	12.425 mM^{-1} s^{-1} (3T)	Breast cancer (MCF-7); cervical cancer (HeLa)	Ma et al.[60]
	PTTA-Eu^{3+}-FA	50 nm	28.98 mM^{-1} s^{-1}	Breast cancer (4T1, MCF-7); cervical cancer (HeLa)	Yue et al.[61]
	GO	3.05 nm	n/a	NSCLC (LLC, H60, H1975 and A549) Cervical cancer (HeLa)	Chen et al.[62]
	MGO/FU-MI	243.6 nm	n/a	NSCLC (H1975 and A549)	Peng et al.[63]
	MnO	12 nm	60.8 mM^{-1} s^{-1}	Liver cell (L02) cancer (HepG2); breast cancer; (4T1); cervical cancer (HeLa)	Yang et al.[52]
	MoS$_2$-FA	3–4 nm	n/a	Breast cancer (4T1); cervical cancer (HeLa); breast cancer (MCF-7); liver cell (L02, BRL-3A)	Zhang et al.[64]
	MFP/GO	5–10 nm	n/a	Lung cell (BEAS-2B); NSCLC (LLC, H1975 and A549)	Peng et al.[65]
	Black phosphorene (BP)/PEI-FA	140 nm	10.078 mM^{-1} s^{-1}	Breast cancer (4T1)	Yao et al.[66]
	FeO$_x$/tamoxifen-PEG (TAM-PEG)	100 nm	5.13 mM^{-1} s^{-1}	Breast cancer (4T1)	Shi et al.[67]
	MnO$_2$/GO$_x$	130 nm	n/a	Breast cancer (4T1)	Kou et al.[68]
Targeting	GO-dimercaptosuccinic acid (DMSA)-PEG-FA	>100 nm	12.425 mM^{-1} s^{-1} (3T)	Breast cancer (MCF-7) Cervical cancer (HeLa) Liver cancer (HepG2)	Yue et al.[69]
Biocompatibility	Cysteamine (Cys)	254 nm	16.9 mM^{-1} s^{-1} (3T)	NSCLC (H1975 and A549)	Sun et al.[45]
	Cysteamine (Cys) Her2 antibody	12 nm	n/a	Bladder cancer	Chou et al.[70]

4.1. Polymer-modified FePt NPs with improved particle dispersion

Slabu et al. mixed hydrophobic FePt NPs with functionalized polymaleic anhydride polymers and dried them to construct hydrophilic FePt NPs that could be redispersed in an aqueous solution.

The preparation process is shown in Fig. 1a.[50] Dynamic light scattering (DLS) analysis showed that the sizes of the FePt NPs coated with amphiphilic polymers were between 7.2 and 14.2 nm regardless of whether the NPs were dispersed in water or PBS, demonstrating the stability of the FePt NPs. Compared to other superparamagnetic iron-based NPs of the same size, the saturation
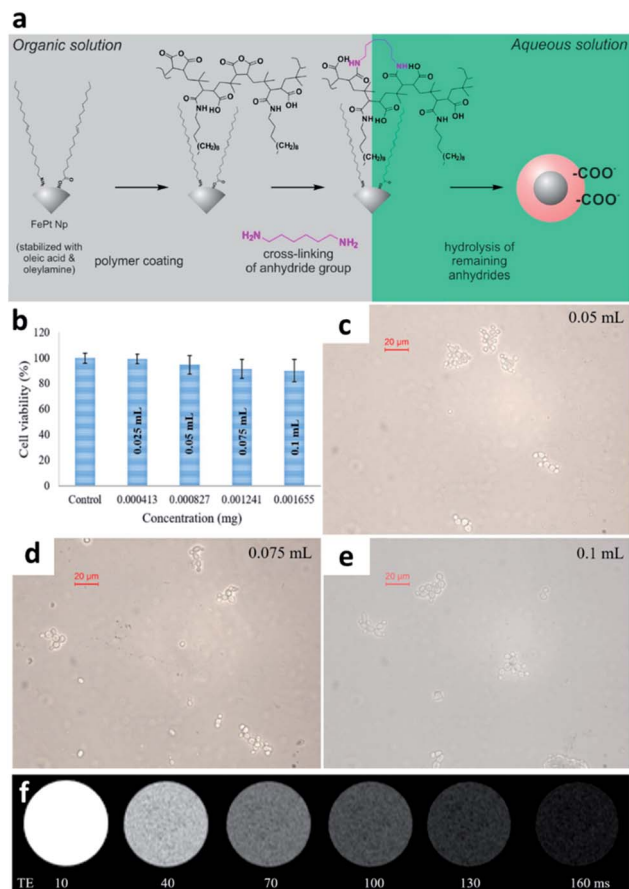
Fig. 1 Organic functional group modification of FePt-CdS NPs. (a) Schematic showing the preparation process of water-soluble FePt NPs and FePt-CdS NPs. (b) Cell compatibility test. Addition of different concentrations of (c) 0.05 mL (d) 0.075 mL and (e) 0.1 mL polymeric FePt NPs. (f) MRI contrast analysis at different FePt NP concentrations. This figure has been reproduced from ref. 50 and 51 with permission from ACS Publications and Elsevier, copyright 2017 and 2019.

magnetization of the polymer-coated FePt NPs increases to approximately 82 A m^2 kg^{-1} Fe as the core size increases slightly. Because the polymer coating makes it difficult to release toxic Pt, the polymer-coated FePt NPs show no apparent cytotoxicity at high concentrations, as shown in Fig. 1b. MRI studies at 1.5T confirmed that for T1 and T2 imaging, the 6 nm polymer-coated FePt NPs are excellent CAs, with an r_2 value of 113 mM^{-1} s^{-1}. According to the authors, additional tests are needed to confirm whether the NPs can be used as MRI CAs. Jha et al. constructed a hydrophilic colloidal bimodal iron-platinum/cadmium-sulfide (FePt-CdS) nanoprobe using a one-pot synthetic method. They modified it with glutathione (GSH), effectively improving the particle dispersion and biocompatibility (Fig. 1c–e).[51] According to the experimental MRI results shown in Fig. 1f, FePt-CdS generates significant T2 contrast, with an r_2 value of 538.1 s^{-1} mg^{-1} mL. Although the lateral relaxation value of FePt-CdS is similar to that of FePt NPs, the CdS quantum dots in the FePt-CdS probe have optical properties that could allow the NPs to be used as cell biomarkers. Therefore, FePt-CdS shows potential as a magnetic and fluorescent nanoprobe for both fluorescence imaging and MRI.[71,72]

4.2. FePt NP composites with MRI-based diagnostic potential

Yang et al. used seed-mediated nucleation to construct MnO and form heterogeneous nuclei at the corners and edges of FePt NPs. The authors then used the solvent exchange to coat the FePt@MnO particles with 1,2-distearoyl-sn-glycero-3-phosphoe-thanolamine-N-[amino(polyethylene glycol)-5000]-folic acid (DSPE-PEG5000-FA) to form 33.65 nm FMDF NPs with improved biological compatibility and dispersibility.[52] The preparation process is shown in Fig. 2a. According to 3T MRI experiments, the
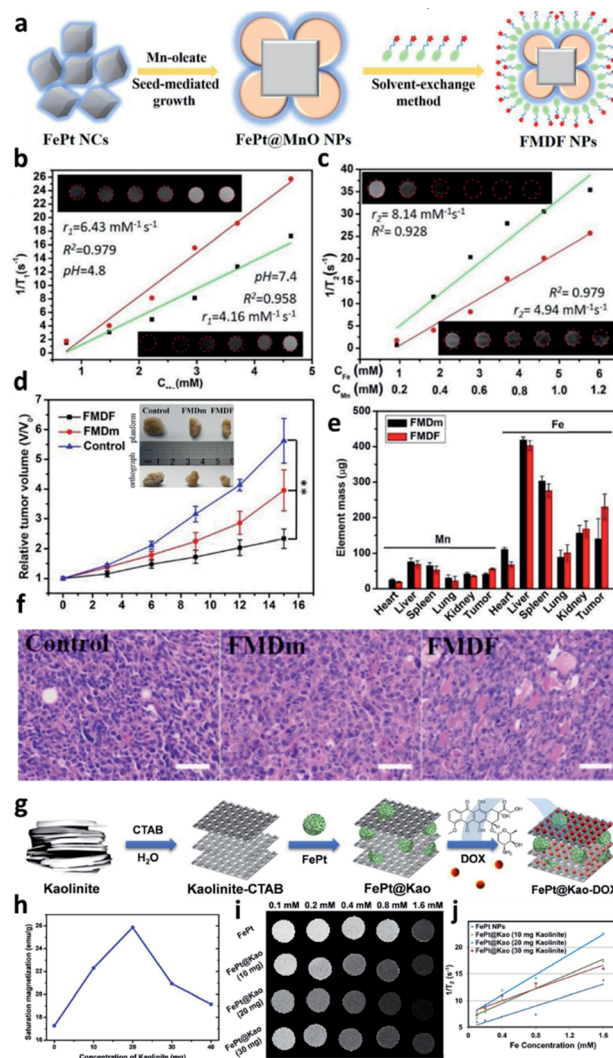

Fig. 2 FePt NPs embedded in organic metal/ceramic fibers. (a) Schematic showing the process used to prepare metal-combined FePt alloy NPs. T2-weighted MRI signals of (b) FePt@MnO NPs and (c) FMDF NPs. (d) Tumor volume results and visible images of FMDF and FMDm NPs. (e) Inductively coupled plasma-mass spectrometry quantification of metal ion accumulation in different tissues. (f) Tumor H&E staining of the control, FMDm (without solvent exchange), and FMDF groups. (g) Schematic showing the preparation process of kaolinite-modified FePt NPs. The MRI results of the kaolinite-modified FePt NPs: (h) saturation magnetization, (i) contrast image, and (j) T2-weighted curve. This figure has been reproduced from ref. 52 and 53 with permission from ACS Publications, copyright 2019 and 2020.

synergistic effect of Mn and Fe greatly enhanced the T2 image contrast, with r_2 reaching 8.14 mM^{-1} s^{-1}. The released Mn^{2+} ions also enhanced the T1-weighted contrast, as shown in Fig. 2b and c. FePt@MnO will release iron and manganese ions into the cell environment after endocytosis. These ions will then interact with antioxidant enzymes such as GSH in the cell, leading to an imbalance in the production and degradation of reactive oxygen species (ROS). This imbalance will trigger the iron-mediated apoptosis reaction (ferroptosis), causing cell death. As shown in Fig. 2d, after intravenous/intratumor injection, the fluorescence was significantly higher in the FMDF NP group than the control group, indicating a sharp increase in the ROS level in the tumor tissue than in the normal tissue. *In vivo* experiments using mouse mammalian gland tumor cells, 4T1-bearing Balb/c mice, revealed that the tumors were inhibited in the FMDF NP group, as shown in Fig. 2e and f. Based on a biodistribution experiment, the position of the cancer was different. The results also proved that the targeting effect of FMDF could make the NPs accumulate in the tumor tissue.

The aggregation of multi-iron and manganese alloy confirmed folic acid (FA) ability-modified FePt@MnO to target tumors. Kaolinite, a hydrophilic material with many hydroxyl groups on its surface, is widely used to alter iron NPs. Chan *et al.* modified FePt NPs with kaolinite to form a sandwich-like FePt@Kao nanostructure. The bulk kaolinite in FePt@Kao is split into a layered structure by the interface-active agent cetyltrimethylammonium bromide.[53] After ultrasonic and heat treatment, the kaolinite layer gradually peels off into a uniform nanomaterial. Kaolinite has a stable chemical structure, strong adsorption capacity, high biocompatibility, and low toxicity. The layered kaolinite structure can be loaded with many different substances, including chemotherapeutic drugs, doxorubicin (DOX), and FePt NPs. Furthermore, the drug release rate can be controlled through this structure (sandwich-like structure of FePt embedded in kaolinite), as shown in Fig. 2g. FePt NPs containing DOX was loaded into the layered space of 20 mg kaolinite to make it highly concentrated in composite NPs. The FePt NPs are subjected to uniaxial compression perpendicular to the montmorillonite layer, and the mechanical stress causes the FePt NPs to form magnetic dipoles. This phenomenon causes the NPs to rearrange so that they are parallel to the direction of compressive stress. Therefore, the saturation magnetization is significantly increased in the magnetization direction, and the MRI signal is also enhanced (r_2 = 29.32 mM^{-1}·s^{-1}; Fig. 2h–j).

4.3. A composite composed of two iron nanomaterials for obtaining stable MRI images

Strong magnetization is one of the necessary conditions for obtaining strong MRI contrast. Although metallic NPs have high magnetization energy, they are easily oxidized in biological environments, resulting in instability. Gao *et al.* found that coating metal NPs with a layer of polycrystalline Fe_2O_3 or Fe_3O_4 can significantly improve their stability.[73] Liu *et al.* developed FePt@Fe_2O_3 core–shell magnetic NPs with FePt NPs as the core and Fe_2O_3 as the shell; PEG-FA was added to reduce cytotoxicity

Fig. 3 Two-component iron nanocomposite for obtaining stable MRI images. (a) Schematic showing the process used to prepare FePt/Fe_3O_4 nanocomposites for conjugation with polymers. (b) T2-weighted MRI contrast image of FePt/Fe_3O_4 nanocomposites. (c) Quantification of MRI contrast. (d) Concentration course of FePt/Fe_3O_4 nanocomposites in MRI analysis. (e and k) The r_2 slope of the concentration-dependent curve. (f) *In vivo* tumor monitoring for different injection times. (g) *In vitro* cell viability and (h) lactate dehydrogenase (LDH) leakage as a function of FePt/Fe_3O_4 nanocomposite concentration. (i) *In vivo* tumor size evaluation with magnetic treatment. (j) Fourier transform infrared spectroscopy characterization results of functional surface ligands. This figure has been reproduced from ref. 56 with permission from Future Science, copyright 2015.

and non-specific binding.[46] The addition of FA allows the effective targeting of folate receptor-positive cancer cells such as papilloma KB cells (Fig. 3a–c). Based on DLS analysis, the FePt@Fe_2O_3-PEG NPs have a size of approximately 51 nm. Fig. 3d and e show that as the iron concentration increased, the T2-weighted MRI image became darker (T2 relaxation rate = 91.9 mM^{-1} s^{-1}). The intravenous injection of the FePt@Fe_2O_3-PEG NPs into Balb/c mice significantly reduced the T2-weighted signal intensity of the tumor. *In vivo* experiments demonstrated that the FePt@Fe_2O_3-PEG NPs provide obvious tumor contrast (Fig. 3f). According to the results of cell viability and mouse experiments, when applied to treat KB cells, high concentrations of the FePt@Fe_2O_3-PEG NPs did not produce any apparent cytotoxicity or cell membrane damage (Fig. 3g and h). Yang *et al.* used PEG-FePt@Fe_3O_4 MNPs to treat mouse breast cancer. MNPs with PEG chains can increase the internalization ratio of NPs, prompt the therapeutic effect, improve the image contrast of tumors, and induce tumor cell death through local temperature increases.[57]

The application of PEG-MNPs significantly reduced the tumor volume; after repeated hyperthermia for two weeks, the tumor was approximately 4.5 times smaller than the control. Yang *et al.* successfully applied FePt@Fe_3O_4 NPs with hyperthermia to slow tumor growth for cervical cancer treatment, as shown in Fig. 3i.

The therapeutic effect is primarily attributed to the high magnetic heat transfer capacity of the PEG-MNPs, which causes thermal ablation and enhances the anti-tumor effect.[56] Kim *et al.* found that 3,4-dihydroxyphenylacetic acid (DOPAC) was a better ligand than dimercaptosuccinic acid (DMSA) for

functionalizing FePt@Fe$_3$O$_4$ core–shell NPs.[58] Compared to DMSA, DOPAC undergoes fewer oxidation reactions, increasing the magnetization energy (Fig. 3j). As shown in Fig. 3k, DOPAC-FePt@Fe$_3$O$_4$ results in T2 contrast enhancement with an r_2 of 131.5 mM^{-1} s^{-1}, suggesting that DOPAC-FePt@Fe$_3$O$_4$ is a potential tool for magnetic hyperthermia.

4.4. Composite FePt NPs for enhancing the therapeutic effect

Under an external magnetic field, free electrons can be excited on the surfaces of FePt NPs. This process releases thermal energy *via* magnetothermal conversion, which causes cancer cells to enter the apoptotic process. Thus, FePt NPs can not only be used for T2-weighted MRI diagnosis, but they can also be used simultaneously for treatment based on the production of magnetic heat, which is called magnetic fluid hyperthermia (MFH).[74] Kostevšek (2018) *et al.* coated multinuclear FePt NPs with SiO$_2$ followed by a two-step inoculation with Au, thereby enhancing the heat generation of the nanosystem.[59] Coating the FePt NPs with SiO$_2$ can improve the biocompatibility of the NPs. Lai *et al.*, who previously coated FePt NPs with silica to enhance biocompatibility, also used this synthetic method.
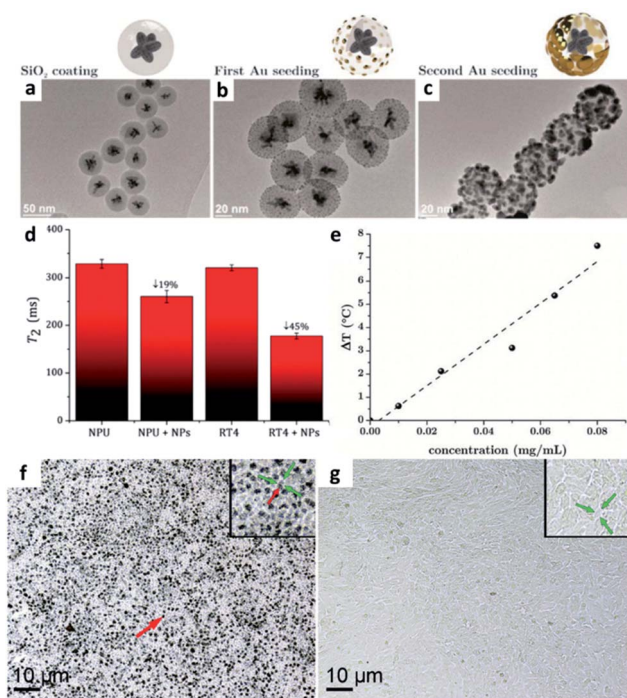

Fig. 4 Integration of inorganic metal materials with FePt NPs. Transmission electron microscopy images of (a) silica-coated FePt NPs, (b) FePt@SiO$_2$ NPs after single Au seeding, and (c) FePt@SiO$_2$ NPs after double Au seeding. (d) Quantification of the T2-weighted MRI signals corresponding to the uptake of different NPs in different cell lines. (e) The heating ability demonstrates the concentration-dependent curve. (f) Internalization of more NPs in tumor cells than (g) normal porcine urothelial (NPU) cells. This figure has been reproduced from ref. 59 with permission from the Royal Society of Chemistry, copyright 2018.

The transmission electron microscopy images of FePt NPs shown in Fig. 4a–c show that the FePt cores were coated with SiO$_2$ to form FePt/SiO$_2$ NPs with an average diameter of 40 ± 3 nm. Au seed crystals of approximately 1–3 nm were formed on the SiO$_2$ surface during the first Au seeding step. After the second Au seeding step, Au particles of 6–10 nm size were found on the SiO$_2$ surface. The longitudinal (T1) and transverse (T2) relaxation rates of the SiO$_2$-coated multicore FePt NPs were 1.5 times lower than those of the FePt NPs without SiO$_2$. However, when the FePt/SiO$_2$/Au NPs were modified with PEG, the coating thickness increased, and the r_2 value decreased by approximately 1.85 times. Due to the significant distance between the water protons and the superparamagnetic core, the magnetic field decreased as the distance from the core material increased. In turn, the relaxation time decreased, affecting the r_1 and r_2 values, as demonstrated by *in vitro* MRI experiments (Fig. 4d). In addition, modifying the surfaces of the FePt NPs with Au could effectively improve the photothermal reaction. As shown in Fig. 4e, as the concentration of FePt/SiO$_2$/Au NPs increased, the heating rate increased linearly, demonstrating the potential of the FePt/SiO$_2$/Au NPs as photothermal agents. According to the *in vitro* cell model analysis, poorly differentiated cancer cells underwent more vital endocytosis than well-differentiated normal urothelial cells. The results indicate that transitional-cell papilloma RT4 cells can internalize more NPs than normal porcine urothelial (NPU) cells (Fig. 4f and g). Thus, the hybrid NPs show high selectivity for cancer cells, demonstrating their excellent potential for cancer diagnosis and the development of anti-cancer therapies in the future.

4.5. Modification with active targeting molecules enhances the accumulation of FePt NPs in tumors

The use of amphiphiles to modify the surfaces of FePt NPs is one of the most effective and widely used methods to improve the dispersibility of MNPs. Modification with amphiphiles can ameliorate the reduced magnetic effect and cytotoxicity caused by the aggregation of NPs with only hydrophilic coatings. Yue *et al.* loaded PEG and FA on graphene oxide (GO), with abundant carboxyl and hydroxyl groups on the surface, making it stable in an aqueous solution. The researchers then loaded FePt-DMSA on the GO nanosheets to form FePt-DMSA/GO-PEG-FA NPs.[69] The T2-weighted image shows an inverse concentration-dependent MRI contrast, and the r_2 value is 12.425 mM^{-1} s^{-1}, suggesting that the FePt/GO composite nanoassemblies are good MRI CA candidates.

Moreover, since FA receptors are highly expressed in malignant tumor cells, the FePt-DMSA/GO-PEG-FA NPs strongly accumulate in breast cancer MCF-7 cells (Fig. 5a–c). At the low pH of the tumor environment, iron ions are released and catalyze ROS formation, inducing cell death. To confirm the therapeutic effect of the NPs, mimicked human 4T1 breast cancer cells were planted under the skin of mice. The tumors were significantly inhibited by treatment with the FePt/GO composite nanoassemblies, as shown in Fig. 5d. The difference in the tumor size after nanocomposite treatment can be seen in the T2 MRI image (Fig. 5e).

Fig. 5 Fluorescent markers track FePt nanomaterials and confirm their therapeutic effects. Confocal images showed (a) the bright field under cell viewpoint with a confocal microscope and (b) the uptake of fluorescent FePt NPs. (c) An image merging (a) and (b). (d) Evaluation of tumor size over time and (e) visual images of the tumors in different treatment groups. This figure has been reproduced from ref. 69 with permission from ACS Publications, copyright 2017.

4.6. Modification of FePt NPs with organic molecules to enhance biocompatibility

Although coating the surfaces of FePt NPs with iron oxide and other inorganic materials can effectively improve the MRI image contrast, doubts remain about whether NPs with exogenous coatings can be delivered to normal tissues and organs. Moreover, iron oxide has the disadvantage of being easily corroded. Therefore, many researchers have coated FePt NPs with

Fig. 6 Modification of FePt NPs with organic molecules to increase biocompatibility and enhance the MRI signal. (a) Schematic showing the transformation of FePt nanocomposites with anti-Her2 monoclonal antibody. (b) Magnetic susceptibility analysis and (c) T2-weighted MRI results obtained with 3 mm and 12 nm FePt-anti-Her2 NPs. (d) T2-weighted MRI results with cysteine marking the concentration-dependent FePt NPs. (e) The r_2 slope of the concentration-dependent curve of FePt NPs. This figure has been reproduced from ref. 45 with permission from Elsevier, copyright 2018.

biological molecules that do not have any safety concerns. Chou *et al.* modified the FePt NP surface with cysteamine (Cys) to improve cell endocytosis.[70]

The exposed amine groups are connected to anti-Her2 antibodies, allowing the targeting of cancer cell lines with high Her2/neu expression, as shown in Fig. 6a. The experimental results in Fig. 6b and c show that the 12 nm FePt-anti-Her2 NPs have high magnetic susceptibility and significant MRI contrast. Other researchers have also applied Cys as a biosafety modification. Sun *et al.* prepared FePt-Cys NPs with a size of approximately 254 nm. The T2-weighted images (Fig. 6d and e) show iron concentration-dependent image contrast. Although the r_2 value of the FePt-Cys NPs is not as high as FePt NPs only, the coating of iron with other molecules can avoid the surface of FePt-NPs to oxidize. Still, the use of these NPs provides good biocompatibility and is less likely to damage the part applied to the brain tissue.[45]

5. Conclusion & future perspectives

We have reviewed progress in the modification of FePt NPs over the past few years. FePt NPs are attractive nanoplatforms with high magnetization values and higher stability than other metal NPs.[66,75] Many studies have demonstrated that FePt NPs can enhance the contrast of MRI images. However, surface coatings are needed to improve particle dispersion and reduce toxicity under physiological conditions. Efficient surface coatings can also increase the T2 contrast of FePt NPs to facilitate diagnostic analysis.

Encapsulating FePt NPs in amphiphilic polymers can prevent them from aggregating and releasing ferroportin ions in aqueous environments,[76] thus helping in maintaining the magnetization value and increasing the biocompatibility and safety of the FePt NPs. Therefore, one of the most basic methods to modify FePt NPs is to coat them with amphiphilic polymers. Coating FePt NPs with Au, SiO_2, GO, and biodegradable polymers can also effectively improve the stability of the FePt NPs. Furthermore, the safety of the NPs can be improved by modification with amino acids, allowing the NPs to be used in diagnosis and therapy for conditions such as brain tumors. However, FePt NPs have the disadvantage of being quickly oxidized; modifying the FePt NPs with iron oxide can stabilize their structures, increase the magnetization, and enhance the T2 MRI contrast. Moreover, kaolinite-based FePt NPs with sandwich-like designs can alter the magnetic dipole arrangement of iron and platinum to increase the saturation magnetization and effectively improve the MRI image intensity.[64,65,77]

FePt NPs can convert superparamagnetism into ferromagnetism through rapid changes in the magnetic field, resulting in the loss of magnetic energy and heat energy generation (*i.e.*, the MFH effect). Based on the sensitivity of tumors to heat, exploring whether NPs can serve as local heating agents is an attractive strategy. The modification of FePt NPs with folate or antibodies can allow the NPs to specifically target tumors. When the NPs are concentrated at the tumor site, they can also effectively improve the T2 contrast at the tumor location. Chemotherapeutic drugs can also be loaded into FePt NPs to

enhance their therapeutic effect in combination with the magnetocaloric response. These FePt NPs show promise as new diagnostic nanoplatforms in medicine. The theranostic application of FePt NPs requires a comprehensive nanocomposite platform for biomedical imaging. Thus, FePt NPs have potential therapeutic value based on their ability to provide real-time feedback to patients with different cancer types.

Author contributions

Z. X. C. and C. H. L. contributed equally to write this review article. M. H. C. and M. H. designed the outline of the review. Y. C. C., C. Y. H., C. H. L., M. H. C. and M. H. performed the correction and revision of the manuscript. M. H. supervised the study. All authors have approved the final version of the manuscript.

Conflicts of interest

There are no conflicts to declare.

Acknowledgements

References

1 C. Nikolaidou, K. Kouskouras, N. Fragakis, V. P. Vassilikos, H. Karvounis and T. D. Karamitsos, *Diagnostics*, 2021, **11**, 1109.

2 F. Maccioni, A. Bruni, M. C. Colaiacomo, E. Angelucci, A. Cocco and R. Caprilli, *Inflammatory Bowel Dis.*, 2006, **12**, S27–S28.

3 T. Bjerner, G. Wikstrom, L. Johansson and H. Ahlstrom, *Invest. Radiol.*, 2004, **39**, 470–478.

4 Y. O. Uca, D. Hallmann, B. Hesse, C. Seim, N. Stolzenburg, H. Pietsch, J. Schnorr and M. Taupitz, *Mol. Imaging Biol.*, 2021, **23**, 382–393.

5 X. D. Xue, R. N. Bo, H. J. Qu, B. Jia, W. W. Xiao, Y. Yuan, N. Vapniarsky, A. Lindstrom, H. Wu, D. L. Zhang, L. M. Li, M. Ricci, Z. Ma, Z. Zhu, T. Y. Lin, A. Y. Louie and Y. P. Li, *Biomaterials*, 2020, **257**, 120234.

6 H. Lee, A. Shahrivarkevishahi, J. L. Lumata, M. A. Luzuriaga, L. M. Hagge, C. E. Benjamin, O. R. Brohlin, C. R. Parish, H. R. Firouzi, S. O. Nielsen, L. L. Lumata and J. J. Gassensmith, *Chem. Sci.*, 2020, **11**, 2045–2050.

7 S. Grahl, M. Bussas, V. Pongratz, J. S. Kirschke, C. Zimmer, A. Berthele, B. Hemmer and M. Muhlau, *Clin. Neuroradiol.*, 2021, **31**, 235–243.

8 B. Mehravi, A. M. Alizadeh, S. Khodayari, H. Khodayari, K. Ashtari, M. Mohseni, N. I. Anaraki, E. A. Dana, S. Safari and M. Amanlou, *Mol. Imaging Biol.*, 2017, **19**, 522–530.

9 G. Conte, S. Casale, L. Caschera, F. M. Lo Russo, C. Paolella, C. Cinnante, F. Di Berardino, D. Zanetti, D. Stocchetti,

10 Y. P. Yew, K. Shameli, M. Miyake, N. B. B. A. Khairudin, S. E. B. Mohamad, T. Naiki and K. X. Lee, *Arabian J. Chem.*, 2020, **13**, 2287–2308.

11 L. S. Ganapathe, M. A. Mohamed, R. M. Yunus and D. D. Berhanuddin, *Magnetochemistry*, 2020, **6**, 68.

12 M. A. Dheyab, A. A. Aziz, M. S. Jameel, O. Abu Noqta, P. M. Khaniabadi and B. Mehrdel, *Sci. Rep.*, 2020, **10**, 10793.

13 S. H. Sun, C. B. Murray, D. Weller, L. Folks and A. Moser, *Science*, 2000, **287**, 1989–1992.

14 M. Mouawad, H. Biernaski, M. Brackstone, M. Lock, A. Kornecki, O. Shmuilovich, I. Nachum, F. Prato, R. Thompson, S. Gaede and N. Gelman, *Med. Phys.*, 2018, **45**, E407.

15 B. Van der Velden, T. Bismeijer, S. Canisius, C. Loo, E. Lips, J. Wesseling, M. Viergever, L. Wessels and K. Gilhuijs, *Eur. J. Cancer*, 2018, **92**, S49–S50.

16 R. Nakamura, N. Yamamoto, A. Yoshii and M. Itami, *Cancer Res.*, 2013, **73**, LB-131.

17 M. H. Chan, W. Chen, C. H. Li, C. Y. Fang, Y. C. Chang, D. H. Wei, R. S. Liu and M. Hsiao, *ACS Appl. Mater. Interfaces*, 2021, **13**, 26759–26769.

18 T. L. Tsai, Y. H. Lai, H. H. W. Chen and W. C. Su, *Int. J. Nanomed.*, 2021, **16**, 2071–2085.

19 W. Chen, M. H. Chan and M. Hsiao, *FASEB J.*, 2020, **34**(S1), 1.

20 S. L. Han, X. Liang, T. Li, F. F. Yin and J. Cai, *Quant. Imaging. Med. Surg.*, 2021, **11**, 32–42.

21 R. Kumar, G. S. Narayanan, B. Vishwanthan, S. Narayanan and S. Mandal, *Pract. Radiat. Oncol.*, 2020, **25**, 1011–1016.

22 L. Koivula, F. Guerreiro, B. W. Raaymakers and J. Korhonen, *Radiother. Oncol.*, 2018, **127**, S1145–S1146.

23 T. Tanaka, R. Tanaka, A. W. K. Yeung, M. M. Bornstein, S. Nishimura, M. Oda, M. Habu, O. Takahashi, D. Yoshiga, T. Sago, I. Miyamoto, M. Kodama, N. Wakasugi-Sato, S. Matsumoto-Takeda, T. Joujima, Y. Miyamura and Y. Morimoto, *Oral Surg., Oral Med., Oral Pathol.*, 2020, **130**, 583–592.

24 F. Aigner, L. Pallwein, M. Schocke, L. Andrei, D. Junker, G. Schafer, G. Mikuz, F. Pedross, W. Horninger, W. Jaschke, E. J. Halpern and F. Frauscher, *J. Ultrasound Med.*, 2011, **30**, 643–649.

25 E. Shevchenko, D. Talapin, A. Kornowski, F. Wiekhorst, J. Kotzler, M. Haase, A. Rogach and H. Weller, *Adv. Mater.*, 2002, **14**, 287–290.

26 B. Wu, K. Deng, S. T. Lu, C. J. Zhang, Y. W. Ao, H. Wang, H. Mei, C. X. Wang, H. B. Xu, B. Hu and S. W. Huang, *Biomaterials*, 2021, **268**, 120531.

27 C. J. Bond, G. E. Sokolow, M. R. Crawley, P. J. Burns, J. M. Cox, R. Mayilmurugan and J. R. Morrow, *Inorg. Chem.*, 2019, **58**, 8710–8719.

28 N. Kostevsek, S. Sturm, I. Sersa, A. Sepe, M. Bloemen, T. Verbiest, S. Kobe and K. Z. Rozman, *J. Nanopart. Res.*, 2015, **17**, 464.

29 E. Kozenkova, K. Levada, M. V. Efremova, A. Omelyanchik, Y. A. Nalench, A. S. Garanina, S. Pshenichnikov, D. G. Zhukov, O. Lunov, M. Lunova, I. Kozenkov,

C. Innocenti, M. Albino, M. A. Abakumov, C. Sangregorio and V. Rodionova, *Nanomaterials*, 2020, **10**, 1646.

30 G. L. Zhang, L. Zhang, Y. C. Si, Q. D. Li, J. M. Xiao, B. Wang, C. Z. Liang, Z. Y. Wu and G. Tian, *Chem. Eng. J.*, 2020, **388**, 124269.

31 Y. G. Wang, X. H. Li, P. Y. Chen, Y. Dong, G. L. Liang and Y. Q. Yu, *Nanoscale*, 2020, **12**, 1886–1893.

32 B. Thangaraj, Z. H. Jia, L. M. Dai, D. H. Liu and W. Du, *Arabian J. Chem.*, 2019, **12**, 4694–4706.

33 J. Lee, J. M. Yoo, Y. Ye, Y. Mun, S. Lee, O. H. Kim, H. W. Rhee, H. I. Lee, Y. E. Sung and J. Lee, *Adv. Energy Mater.*, 2015, **5**, 1402093.

34 A. Delattre, S. Pouget, J. F. Jacquot, Y. Samson and P. Reiss, *Small*, 2010, **6**, 932–936.

35 G. Gupta, M. N. Patel, D. Ferrer, A. T. Heitsch, B. A. Korgel, M. Jose-Yacaman and K. P. Johnston, *Chem. Mater.*, 2008, **20**, 5005–5015.

36 D. Chen, X. Zhao, S. S. Chen, H. F. Li, X. N. Fu, Q. Z. Wu, S. P. Li, Y. Li, B. L. Su and R. S. Ruoff, *Carbon*, 2014, **68**, 755–762.

37 Z. Kang, Y. S. Peng, L. X. Zhou, Z. M. Li, T. Y. Wang, Z. Zhang, Q. L. Liao, J. Gao, Y. N. Li and Y. Zhang, *Mater. Chem. Front.*, 2018, **2**, 1609–1617.

38 T. Fuchigami, R. Kawamura, Y. Kitamoto, M. Nakagawa and Y. Namiki, *Biomaterials*, 2012, **33**, 1682–1687.

39 T. Fuchigami, R. Kawamura, Y. Kitamoto, M. Nakagawa and Y. Namiki, *Langmuir*, 2011, **27**, 2923–2928.

40 Y. P. Liu, Q. Y. Xia, Y. Liu, S. Y. Zhang, F. Cheng, Z. H. Zhong, L. Wang, H. X. Li and K. Xiao, *Nanotechnology*, 2014, **25**, 425101.

41 Y. J. Kang, M. Uchida, H. H. Shin, T. Douglas and S. Kang, *Soft Matter*, 2011, **7**, 11078–11081.

42 X. Jiang, S. Weise, M. Hafner, C. Rocker, F. Zhang, W. J. Parak and G. U. Nienhaus, *J. R. Soc., Interface*, 2010, **7**, S5–S13.

43 M. Rigol, N. Solanes, M. Roque, J. Farre, M. Batle, S. Roura, N. Bellera, C. Prat-Vidal, A. Sionis, J. Ramirez, M. Sitges, G. Sanz, A. Bayes-Genis and M. Heras, *Transplant. Proc.*, 2008, **40**, 3619–3622.

44 Y. B. Liu, P. C. Wu, S. Guo, P. T. Chou, C. X. Deng, S. W. Chou, Z. Yuan and T. M. Liu, *Photoacoustics*, 2020, **19**, 100179.

45 Y. M. Sun, H. T. Miao, S. J. Ma, L. Zhang, C. C. You, F. Tang, C. Yang, X. L. Tian, F. Wang, Y. Luo, X. J. Lin, H. Wang, C. Y. Li, Z. J. Li, H. N. Yu, X. F. Liu, Y. Xiao, Y. Gong, J. H. Zhang, H. Quan and C. H. Xie, *Cancer Lett.*, 2018, **418**, 27–40.

46 Y. M. Liu, K. Yang, L. Cheng, J. Zhu, X. X. Ma, H. Xu, Y. G. Li, L. Guo, H. W. Gu and Z. Liu, *J. Nanomed. Nanotechnol.*, 2013, **9**, 1077–1088.

47 S. Chen, L. J. Wang, S. Brown, D. Cole-Hamilton, S. Lee, A. Melzer, A. Cuschieri and P. Andre, *Abstr. Pap. Am. Chem. Soc.*, 2009, **238**, 500–COLL.

48 K. McNamara and S. A. M. Tofail, *Adv. Phys.: X*, 2017, **2**, 54–88.

49 M. Bystrzejewski and M. H. Rummeli, *Pol. J. Chem.*, 2007, **81**, 1219–1255.

50 I. Slabu, K. Wiemer, J. Steitz, R. Liffmann, B. Mues, S. Eisold, T. Caumanns, J. Mayer, C. K. Kuhl, T. Schmitz-Rode and U. Simon, *Langmuir*, 2019, **35**, 10424–10434.

51 D. K. Jha, K. Saikia, S. Chakrabarti, K. Bhattacharya, K. S. Varadarajan, A. B. Patel, D. Goyary, P. Chattopadhyay and P. Deb, *Mater. Sci. Eng., C*, 2017, **72**, 415–424.

52 B. C. Yang, Q. Y. Liu, X. X. Yao, D. S. Zhang, Z. C. Dai, P. Cui, G. R. Zhang, X. W. Zheng and D. X. Yu, *ACS Appl. Mater. Interfaces*, 2019, **11**, 38395–38404.

53 M. H. Chan, M. R. Hsieh, R. S. Liu, D. H. Wei and M. Hsiao, *Chem. Mater.*, 2020, **32**, 697–708.

54 Z. F. Hu, Z. C. Dai, X. W. Hu, B. C. Yang, Q. Y. Liu, C. H. Gao, X. W. Zheng and Y. Q. Yu, *J. Nanobiotechnol.*, 2019, **17**, 38.

55 Y. F. Meng, D. S. Zhang, X. Chen, Z. C. Dai, X. X. Yao, P. Cui, D. X. Yu, G. R. Zhang and X. W. Zheng, *ACS Appl. Nano Mater.*, 2020, **3**, 4494–4503.

56 Q. H. Yang, M. G. Gong, S. Cai, T. Zhang, J. T. Douglas, V. Chikan, N. M. Davies, P. Lee, I. Y. Choi, S. Q. Ren and M. L. Forrest, *Ther. Delivery*, 2015, **6**, 1195–1210.

57 M. D. Yang, C. H. Ho, S. Ruta, R. Chantrell, K. Krycka, O. Hovorka, F. R. Chen, P. S. Lai and C. H. Lai, *Adv. Mater.*, 2018, **30**, 1802444.

58 D. H. Kim, Y. Tamada, T. Ono, S. D. Bader, E. A. Rozhkova and V. Novosad, *J. Nanosci. Nanotechnol.*, 2014, **14**, 2648–2652.

59 N. Kostevšek, I. Abramovic, S. Hudoklin, M. E. Kreft, I. Sersa, A. Sepe, J. Vidmar, S. Sturm, M. Spreitzer, J. Scancar, S. Kobe and K. Z. Rozman, *Nanoscale*, 2018, **10**, 1308–1321.

60 S. J. Ma, H. T. Miao, Y. Luo, Y. M. Sun, X. L. Tian, F. Wang, C. C. You, S. Peng, G. L. Tang, C. Yang, W. J. Sun, S. Y. Li, Y. L. Mao, J. Y. Xu, Y. Xiao, Y. Gong, H. Quan and C. H. Xie, *Int. J. Biol. Sci.*, 2019, **15**, 999–1009.

61 L. D. Yue, Z. C. Dai, X. Chen, C. M. Liu, Z. F. Hu, B. Song and X. W. Zheng, *Nanoscale*, 2018, **10**, 17858–17864.

62 M. M. Chen, B. C. Yang, J. L. Zhu, H. Liu, X. Zhang, X. W. Zheng and Q. Y. Liu, *Mater. Sci. Eng., C*, 2018, **90**, 610–620.

63 X. Peng, C. Yang, X. Kong, Y. Xiang, W. Dai and H. Quan, *Clin. Transl. Oncol.*, 2020, **22**, 1875–1884.

64 D. S. Zhang, P. Cui, Z. C. Dai, B. C. Yang, X. X. Yao, Q. Y. Liu, Z. F. Hu and X. W. Zheng, *Nanoscale*, 2019, **11**, 19912–19922.

65 S. Peng, Y. M. Sun, Y. Luo, S. J. Ma, W. J. Sun, G. L. Tang, S. Y. Li, N. N. Zhang, J. B. Ren, Y. Xiao, X. F. Liu, J. H. Zhang, Y. Gong and C. H. Xie, *Int. J. Biol. Sci.*, 2020, **16**, 2145–2158.

66 X. X. Yao, B. C. Yang, S. Wang, Z. C. Dai, D. S. Zhang, X. W. Zheng and Q. Y. Liu, *J. Mater. Chem. B*, 2020, **8**, 8010–8021.

67 L. N. Shi, Y. J. Wang, C. Zhang, Y. Zhao, C. Lu, B. L. Yin, Y. Yang, X. Y. Gong, L. L. Teng, Y. L. Liu, X. B. Zhang and G. S. Song, *Angew. Chem., Int. Ed.*, 2021, **60**, 9562–9572.

68 Y. K. Kou, Z. C. Dai, P. Cui, Z. F. Hu, L. Tian, F. F. Zhang, H. Q. Duan, Q. Y. Xia, Q. Y. Liu and X. W. Zheng, *J. Mater. Chem. B*, 2021, **9**, 8480–8490.

69 L. D. Yue, J. L. Wang, Z. C. Dai, Z. F. Hu, X. Chen, Y. F. Qi, X. W. Zheng and D. X. Yu, *Bioconjugate Chem.*, 2017, **28**, 400–409.

70 S. W. Chou, C. L. Liu, T. M. Liu, Y. F. Shen, L. C. Kuo, C. H. Wu, T. Y. Hsieh, P. C. Wu, M. R. Tsai, C. C. Yang, K. Y. Chang, M. H. Lu, P. C. Li, S. P. Chen, Y. H. Wang, C. W. Lu, Y. A. Chen, C. C. Huang, C. R. C. Wang, J. K. Hsiao, M. L. Li and P. T. Chou, *Biomaterials*, 2016, **85**, 54–64.

71 J. S. Son, J. S. Lee, E. V. Shevchenko and D. V. Talapin, *J. Phys. Chem. Lett.*, 2013, **4**, 1918–1923.

72 S. L. He, H. W. Zhang, S. Delikanli, Y. L. Qin, M. T. Swihart and H. Zeng, *J. Phys. Chem. C*, 2009, **113**, 87–90.

73 Y. Gao, X. W. Zhang, Z. G. Yin, S. Qu, J. B. You and N. F. Chen, *Nanoscale Res. Lett.*, 2010, **5**, 1–6.

74 M. Lin, Y. H. Xiao, X. M. Jiang, J. Zhang, T. Guo and Y. J. Shi, *J. Nanomater.*, 2020, **2020**, 7180613.

75 A. Stegarescu, S. Gutoiu, I. Lung, O. Opris, C. Leostean, O. Pana, L. Barbu and M. L. Soran, *J. Nanopart. Res.*, 2021, **23**, 91.

76 Y. P. Pan, Z. N. Ren, S. Gao, J. M. Shen, L. Wang, Z. C. Xu, Y. Yu, P. Bachina, H. Z. Zhang, X. Fan, A. Laganowsky, N. Yan and M. Zhou, *Nat. Commun.*, 2020, **11**, 5686.

77 Y. F. Meng, D. S. Zhang, Y. Q. Sun, Z. C. Dai, T. T. Zhang, D. X. Yu, G. R. Zhang and X. W. Zheng, *J. Mater. Chem. B*, 2020, **8**, 11021–11032.